

# Deep and wide field imaging of the Coma cluster: the data<sup>\*</sup>

C. Adami<sup>1</sup>, J.P. Picat<sup>2</sup>, C. Savine<sup>1</sup>, A. Mazure<sup>1</sup>, M.J. West<sup>3</sup>, J.C. Cuillandre<sup>4</sup>, R. Pelló<sup>2</sup>, A. Biviano<sup>5</sup>, C.J. Conselice<sup>6</sup>, F. Durret<sup>7,8</sup>, J.S. Gallagher III<sup>9</sup>, M. Gregg<sup>10</sup>, C. Moreau<sup>1</sup>, and M. Ulmer<sup>11</sup>

<sup>1</sup> LAM, Traverse du Siphon, 13012 Marseille, France

<sup>2</sup> Observatoire Midi-Pyrénées, 14 Av. Edouard Belin, 31400 Toulouse, France

<sup>3</sup> Department of Physics and Astronomy, University of Hawaii, 200 West Kawili Street, Hilo HI 96720-4091, USA

<sup>4</sup> Canada-France-Hawaii Telescope Corporation, 65-1238 Mamalahoa Highway, Kamuela, HI 96743

<sup>5</sup> INAF/Osservatorio Astronomico di Trieste, via G.B. Tiepolo, 11, 34131 Trieste, Italy

<sup>6</sup> Department of Astronomy, Caltech, MS 105-24, Pasadena CA 91125, USA

<sup>7</sup> Institut d'Astrophysique de Paris, CNRS, Université Pierre et Marie Curie, 98bis Bd Arago, 75014 Paris, France

<sup>8</sup> Observatoire de Paris, LERMA, 61 Av. de l'Observatoire, 75014 Paris, France

<sup>9</sup> University of Wisconsin, Department of Astronomy, 475 N. Charter St., Madison, WI 53706, USA

<sup>10</sup> Department of Physics, University of California at Davis, 1 Shields Avenue, Davis, CA 95616

<sup>11</sup> Northwestern University, 2131 Sheridan, 60208-2900 Evanston, USA

Accepted . Received ; Draft printed: October 9, 2018

**Abstract.** An abstract should be given

**Key words.** galaxies: clusters: individual (Coma)

## 1. Introduction

Long considered the archetype of rich and relaxed clusters, Coma is now known to have a rather complex structure, with a number of substructures detected at various wavelengths (see Biviano 1998 for a complete review on the Coma cluster up to 1995). Indeed, although a large quantity of multi-wavelength observational data are presently available for Coma, our theoretical understanding of this unique cluster is still far from complete.

Previous photometric studies of the Coma cluster were done in few colors, and were limited either to wide but shallow surveys or to small deep ones, often obtained under less-than-ideal seeing conditions. For example, very large shallow surveys (e.g. Godwin & Peach 1977, hereafter GP77) were the basis for important studies of the Coma cluster luminosity function and of the properties of galaxies in general. However, due to the shallowness of this catalog, very little was known about Coma's galaxy population at magnitudes fainter than  $R \simeq 20$ . Recent deeper catalogs are still limited to  $R \sim 21$  when covering the whole

cluster (e.g. Castander et al. 2001, Terlevich et al. 2001 or Komiyama et al. 2002). Finally, very deep catalogs such as that of Bernstein et al. (1995) covered only a very small area of sky. While many of these previous studies led to important discoveries, all suffered to some extent from insufficient depth or coverage, which made it difficult to generalize the results obtained from these studies.

Here we report a new catalog of Coma cluster galaxies, obtained with the CFH12K camera (Cuillandre et al. 2000) installed at the prime focus of the Canada-France-Hawaii Telescope (CFHT), which provides the first deep, wide-field images of Coma in the B, V, R and I filters, in seeing conditions well below 1 arcsec for a large part of the observations. As the field covered by the CFH12K is  $0.32 \text{ deg}^2$  we made two overlapping pointings to cover a total field of  $0.6 \text{ deg}^2$ . The data obtained are significantly deeper than any of the recent CCD large field imaging of the Coma cluster; e.g. Terlevich et al. 2001 (U and V filters, depth  $V=20$ ,  $1 \text{ deg}^2$ ,  $2.2 \text{ arcsec}$  seeing) or Komiyama et al. 2002 (B and R filters,  $2.25 \text{ deg}^2$ , complete to  $R=21$ , seeing from 0.8 to 1.5 arcsec). A BVR trichromatic image of the final result is shown in Fig. 1.

Our main scientific goals in obtaining deep wide-field multi-color images of Coma are: a) to study environmental effects on the faint end slope of the galaxy luminosity function (as a very significant extension of, e.g., the work by Lobo et al. 1997 or by Andreon & Cuillandre 2002); b) to analyze Coma's morphological and dynamical struc-

<sup>\*</sup> Based on observations obtained at the Canada-France-Hawaii Telescope (CFHT) which is operated by the National Research Council of Canada, the Institut des Sciences de l'Univers of the Centre National de la Recherche Scientifique and the University of Hawaii.

**Fig. 1.** BVR color image of the Coma cluster from our CFH12K data. The size of the field is  $0.72\text{deg}\times 0.82\text{deg}$ . North is up and East is to the left.

ture to see how it relates to the cluster’s formation history (e.g. Mellier et al. 1988 or Adami et al. 2005b), the diffuse light emission (Adami et al. 2005a) and the faint and low surface brightness galaxy distribution (Adami et al., 2006, submitted). However, because this new Coma catalog provides a rich source of data that will undoubtedly be useful for other researchers, we intend to make it publicly available.

In this paper, we describe our data acquisition, reduction, and cataloguing. Catalogs are available at <http://cencosw.oamp.fr/>.

## 2. Observations and data reduction

### 2.1. Requirements

Several considerations guided our survey design; we summarize these below.

Requirement 1: One of our primary science drivers was to investigate environmental effects on the galaxy population in the Coma cluster. Limiting ourselves to the densest part of the cluster, we wanted to cover at least 5 core radii, in order to sample regions where the density falls below  $\sim 1\%$  of the central cluster galaxy density. To do this requires surveying a region  $50\times 50$  arcmin<sup>2</sup>, which is possible with two adjacent CFH12K fields (see next section).

Requirement 2: We study the spectral energy distributions of galaxies in order to constrain galaxy formation models. Four photometric bands were required for this, in order to obtain color-color plots. We also wanted to compute photometric redshifts and this requires, at the cluster redshift, to have at least one band below the  $4000\text{\AA}$  break and one above it. For Coma, this means that we needed U band data (not yet acquired) and B, V, R and I band data (all observed).

Requirement 3: We wanted to sample the dwarf galaxy population as deep as possible in at least one band, without suffering too much contamination from globular clusters. At the redshift of Coma, this implies needing a complete catalog down to  $R=24$  (see Bernstein et al. 1995).

### 2.2. Instrumental setup

Our data were acquired at the CFHT 3.6m telescope with the CFH12K CCD mosaic (12 individual  $2048\times 4096$  CCDs) (see Cuillandre et al. 2000 and Table 1) installed at the prime focus. The pixel size is 0.206 arcsec, well suited to the mean seeing at prime focus ( $\sim 0.8$  arcsec), giving a full field of view of  $42\times 28$  arcmin<sup>2</sup> per field. Two adjacent fields offset in the North/South direction with a  $\sim 7$  arcmin overlap were observed in the B, V, R and I CFH12K filters giving a final field of view of  $0.72\times 0.82$  deg<sup>2</sup> (in good agreement with Requirement 1). The V, R and I are Mould filters while B is a CFH12K customized

**Table 1.** Main characteristics of the detectors

Detector	CFH12K
Pixel size	0.206 arcsec
Gain	$1.4\text{--}1.8$ e <sup>-</sup> /ADU (typically 1.5)
Quantum efficiency	80% at [600,700]nm
Readout noise	3 to 10 e <sup>-</sup> (typically 5)
Dark current	1 e <sup>-</sup> per min

**Table 2.** Filter characteristics

Filter	$\lambda(\text{\AA})$	$\Delta\lambda(\text{\AA})$	Peak transmission
B	4310	950	85%
V	5370	940	90%
R	6580	1300	85%
I	8223	2164	91%

filter (see Table 2). We will refer hereafter to the filters using the capital letters B, V, R and I and to the fields as North for the North pointing and South for the South pointing. These four bands partially satisfy Requirement 2, and we still plan to acquire the missing U band data.

### 2.3. Exposure times and first/second epoch data

A first set of B, V, R observations was obtained in 1999 and 2000 with only 10 of the 12 CCDs available at that time (first epoch data). A second set of CFH12K images (second epoch data) with all CCDs working, was obtained in 2000: the South field only in R, both North and South fields in I. In both runs, long exposures (1 to 2h) were split into several shorter ones, offset by a few arcsec, in order to improve the cosmetics, flat field and fringing corrections. Offsets between exposures were kept small enough so that images could be stacked without correcting for the differential distortion between exposures.

Exposure times were 24 min in B, 12 to 14 min in V, 10 to 12 min in R and 12 min in I, rather long (which resulted in bright galaxies being saturated) in order to be sky background limited and to minimize the overheads. Tables 1, 2, 3 and 4, summarize the main observational informations.

### 2.4. Data reduction

Acquiring and reducing the data was part of C. Savine’s PhD Thesis (Savine 2002) and the process is fully described in her thesis report (available at <http://cencosw.oamp.fr/>). Here we summarize the key steps.

First epoch data were preprocessed by J.C. Cuillandre using his own FITS Large Images Processing Software (FLIPS) package, which performs functions similar to

**Table 3.** First epoch observations

Filter	Field	Center (J2000)	Exposures	Total exposure time (s)	Mean seeing (arcsec)	Observing year
B	South	12:59:40.00 ; 27:48:47.1	5	7200	1.07	2000
B	North	12:59:40.00 ; 28:10:07.0	5	7200	1.01	2000
V	South	12:59:40.00 ; 27:48:47.1	5	4200	1.00	2000
V	North	12:59:40.00 ; 28:10:07.0	7	5040	0.97	2000
R	South	12:59:40.00 ; 27:49:07.2	6	3300	0.90	1999
R	North	12:59:40.00 ; 28:10:06.9	5	3600	0.87	2000

**Table 4.** Second epoch observations

Filter	Field	Center (J2000)	Exposures	Total exposure time (s)	Mean seeing (arcsec)	Observing year
R	South	12:59:40.00 ; 27:49:17.0	10	7200	0.85	2000
I	South	12:59:40.00 ; 27:48:46.9	10	7200	0.80	2000
I	North	12:59:40.00 ; 28:10:06.9	10	7200	1.00	2000

IRAF task MSCRED and is optimised to handle large mosaics.

Second epoch data were fully preprocessed at the TERAPIX (<http://terapix.iap.fr/soft/>) center using FLIPS and then processed with the TERAPIX modules for photometric and astrometric calibrations and mosaic image construction.

In both cases, a ‘superflat’ built from science images on ‘empty’ fields obtained during the same period was used to subtract the fringe patterns. The mosaic is normalised on CCD 04, with the higher sky value. Residual variations are very small and the flat-fielding appears to be good to better than 0.1% in B and V across the full mosaic (Kalirai et al. 2001).

Astrometric and photometric calibration and mosaic image construction were performed for each CCD chip using IRAF routines for first epoch data. The APM catalog (<http://www.ast.cam.ac.uk/apm-cat/>) has been taken as reference to transform the distorted (x,y) positions into corrected ( $\alpha, \delta$ ) coordinates using the IRAF package ‘IMAGE.IMCOORDS’. For second epoch data Terapix modules were used. With Terapix, photometric and astrometric calibrations are determined using the entire mosaic to give more homogeneous solutions. A global astrometric solution for all CCD images projected onto a common system was computed with comparison to the USNO catalog for absolute calibration.

Photometric calibration was performed by comparison to a set of several Landolt fields observed at the same epoch. For each filter, the zero point determination was found to be quite similar for the 12 individual CCDs, with a mean error less than 0.025 magnitude, except for the South first epoch data in the R filter which will be not used in the catalog.

Because the shifts between exposures are small and there are few exposures, gaps between individual CCDs are only partially corrected and present a lower signal-to-noise ratio. However, this affects only a very small fraction

of the surveyed area, and should have little or no effect on most studies based on the catalog.

### 3. The catalog

#### 3.1. Choice of first/second epoch and North/South data

In the final catalog, data for objects with declinations  $\delta \leq +28.05^\circ$  are taken from the South field, while objects with  $\delta \geq +28.05^\circ$  are taken from North data.

On the whole field, the B and V data are only available from first epoch data and the I band data from second epoch data. The R band data are taken from the first epoch in the North and from the second epoch in the South.

#### 3.2. Combination of B, V, R and I data

The BVR catalog for first epoch data was built with reference to the R positions, selecting the nearest object in the other filters, and checking the magnitude consistency. As the astrometric solution was determined CCD by CCD using a low order polynomial function, residual distortions can be large (1 to 3 arcsec) in the corners and at the edges of the individual CCDs, and the proximity criterion is no longer valid for combination with data which do not suffer from the same errors. This is the case for the second epoch data for which a better global astrometric solution on each of the South and North fields was derived.

In order to recover the distorted regions, we developed a more sophisticated geometrical method, searching for the association which minimizes the distances of all objects in a given area around the reference objects. This is a pattern recognition process which is quasi-independent of residual distortions if the area is small compared to the distortion scale. In cases when there were fewer than 2 objects in common in the exploration area, the nearest object was selected. The best combinations (in terms of errors and number of matched objects), confirmed with

a map of the associated positions, was obtained with an exploration area of radius 15 arcsec, allowing for position errors as large as 3 arcsec. At the end of the process, results were checked for possible duplicate associations and corrected.

The final result is a single catalog of more than 60,000 objects (galaxies and point sources) with B, V, R and I data in the area covered by the South and North pointings. The object positions were selected from the R data, from the first epoch in the North and the second epoch from the South.

### 3.3. Catalog content

The following quantities are given in the catalog:

- identification number for each object
- $(\alpha, \delta)$  coordinates in J2000
- aperture magnitudes in the 4 bands for a 3 arcsec aperture
  - SExtractor error estimates on these magnitudes
  - total magnitudes in the 4 bands
  - SExtractor error estimates on these magnitudes
  - SExtractor central surface brightness (in the I and R bands)
    - external magnitude errors in the four bands and for each measured magnitude
    - shape parameters: minor axis, major axis, orientation (in the I and R bands)
    - SExtractor star-galaxy classification (in the I and R bands)
      - our star-galaxy classification in the I band (distinct from the SExtractor one)
      - SExtractor detection flags (see Bertin & Arnouts 1996)
      - B, V, and R magnitudes taken from the literature, scaled to our system for objects brighter than  $R=17.5$

How these parameters were computed is described below.

## 4. Catalog analysis

### 4.1. Object extraction

Sources were extracted using the SExtractor package (Bertin & Arnouts 1996). The detection threshold was set to  $2\sigma$ , a trade off between detecting as many objects as possible and limiting the number of false detections. The minimum number of contiguous pixels above the detection threshold for extraction was set to 9, a conservative value which corresponds to about half of the pixels at FWHM for a 0.9 arcsec seeing. In this way, although we limit our detection of the large surface brightness population, we increase the confidence in the detections.

Aperture magnitudes were calculated, in all filters, using the SExtractor MAGAuto parameter based on the Kron total magnitude. Central surface brightnesses were computed in the best quality bands (R and I) only.

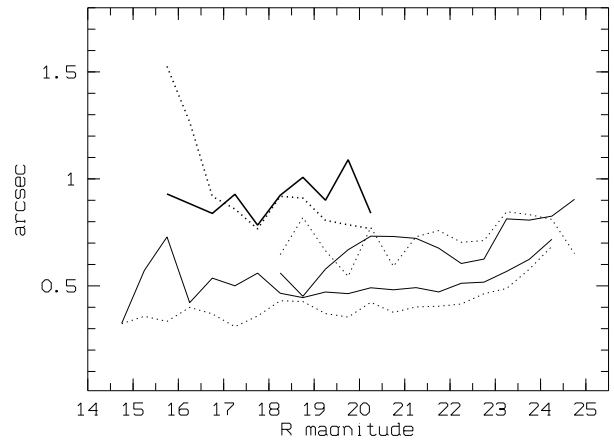


**Fig. 2.** Variation of the astrometric dispersion in  $\alpha$  (solid lines) and  $\delta$  (dashed lines) as a function of R magnitude. From bottom to top: Very thin lines (first two lines): comparison between first and second epoch data. Thin lines (third and fourth lines): comparison with Bernstein et al. (1995). Thick lines (fifth and sixth lines): comparison with GP77.

### 4.2. Internal astrometry

The astrometry was computed on the R band images with an accuracy of about 0.2-0.3 arcsec over the whole field, which is typical of the precision of the reference catalogs, except in the small bands at the edges of the CCDs for the first epoch data.

The relative astrometry with the other filters is much better; for example, in the B band, the residual dispersion is 0.07 arcsec in  $\alpha$  and 0.08 arcsec in  $\delta$ .

Comparison of the astrometric solutions between the two epochs in the common South field and in the R filter shows an agreement at the 0.5 arcsec level (see Fig. 2) for all magnitudes.

### 4.3. Astrometry comparison to published data

For sources brighter than  $R=20$ , the comparison of our catalog positions to those in the USNO and GP77 catalogs shows a dispersion of about 0.75 arcsec with USNO and 0.9 arcsec with GP77 in both  $\alpha$  and  $\delta$ . The astrometry dispersion between our catalog and GP77 is typical of the astrometry error of the GP77 catalog itself.

For sources fainter than  $R=20$ , the comparison of our catalog with that of Bernstein et al. (1995) shows a dispersion of about 0.7 arcsec.

Results are presented in Fig. 2.

### 4.4. Photometric corrections

Zero points were computed using observations of standard stars (Landolt 1992) in the fields SA101, SA104 and SA110. These standards were observed at nearly the same air mass as the science observations in the case of first epoch data and scaled to zero air mass for the second

epoch. The correction in magnitude due to small airmass variations would have been, at maximum, of 0.033 magnitude for R, 0.020 magnitude for V, and 0.015 magnitude for B, much less than the estimated error in the magnitudes, and hence were neglected. We also computed central surface brightnesses in the R and I bands. The calibration was done on the entire mosaic after scaling each chip, assuming identical color equations for all CCDs. This proves to be true at better than 4% for all the CFH12K observations (McCracken et al. 2003). The B, V and R filters appear to have negligible color terms with respect to the Johnson Kron Cousins system and we chose to stay in the CFH12K system, applying no correction in the catalog for the color equations, even in I where the correction could be of the order of  $I=0.1$ . Instrumental magnitudes are converted to the Vega system.

We correct for Galactic extinction using the Schlegel et al. (1998) maps. This contribution remains small:  $\sim 0.05$  magnitude for the B band in the worst case.

#### 4.5. Magnitude error budget

Magnitude errors are due to zero point uncertainties, seeing inhomogeneities and internal errors. These are discussed below.

##### 4.5.1. Computed error budget

Zero point uncertainties are smaller than 0.03 magnitude. In order to check the effects of seeing conditions on the photometry, we compared the aperture magnitudes on R images (0.8 arcsec seeing) to the aperture magnitudes on the same images convolved with a Gaussian to mimic 1.00 arcsec seeing. We confirm the results by Saglia et al (1993): when the seeing gets worse, the objects appear fainter since part of the signal is scattered into the background. The worst error remains smaller than 0.25 magnitudes at  $R\sim 24$ . We note, however, that such a process slightly underestimates the error because of the background smoothing.

Internal SExtractor errors are of the order 0.1 magnitude at  $R\sim 24$ , a large part probably due to close neighbors as shown in the section which describes the catalog properties.

In total, we therefore expect errors for the faintest catalogued objects ( $R\sim 24$ ) to be of the order of  $\sim 0.27$  magnitude.

##### 4.5.2. Externally estimated error budget

To get an external estimate of the magnitude error budget, we used the overlap between the North and South fields in the B, V and I bands and the two South pointings in the R filter. Results based on several thousand objects common to both fields in the overlap region for the B and V filters are shown in Figs. 3 and 4 as a function of magnitude.

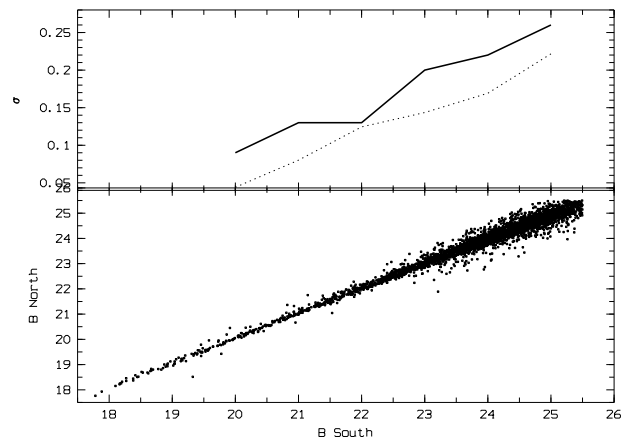


**Fig. 3.** Upper graph: solid line: statistical  $1\sigma$  magnitude uncertainties between the North and South fields, dashed line: quadratic sum of the internal error from SExtractor and of the error due to the different seeing between different observations. Lower graph: B North versus B South magnitudes.

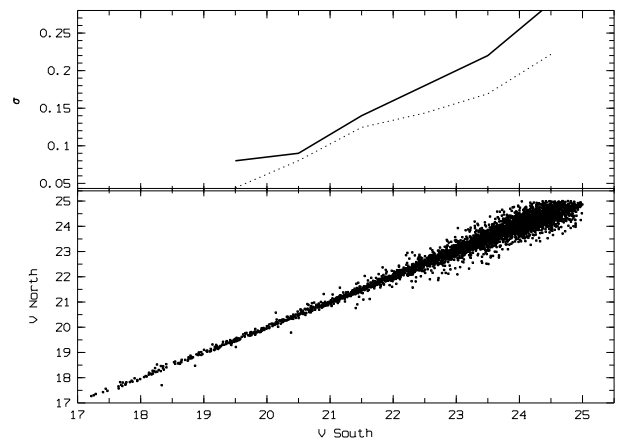


**Fig. 4.** Upper graph: solid line: statistical  $1\sigma$  uncertainties between North and South fields, dashed line: quadratic sum of internal error from SExtractor and error due to the different seeing between different observations. Lower graph: V North versus V South magnitudes.

Results of the two R observations and in the common I area are shown in Fig. 5.

The increasing uncertainty at the bright end in the R and I bands is due to the second epoch data, because of a background over-correction by Terapix near bright objects, and saturation effects on deep images.

From this analysis we can approximate the magnitude dispersion by regression laws for B, V, R and I filters with parameters given in Table 5.

The photometric accuracy is better than 0.3 magnitude in all bands, in good agreement with the computed error budget. Also, the R error estimate is probably an overestimate for the faint part of second epoch data, which are clearly deeper and of better quality.

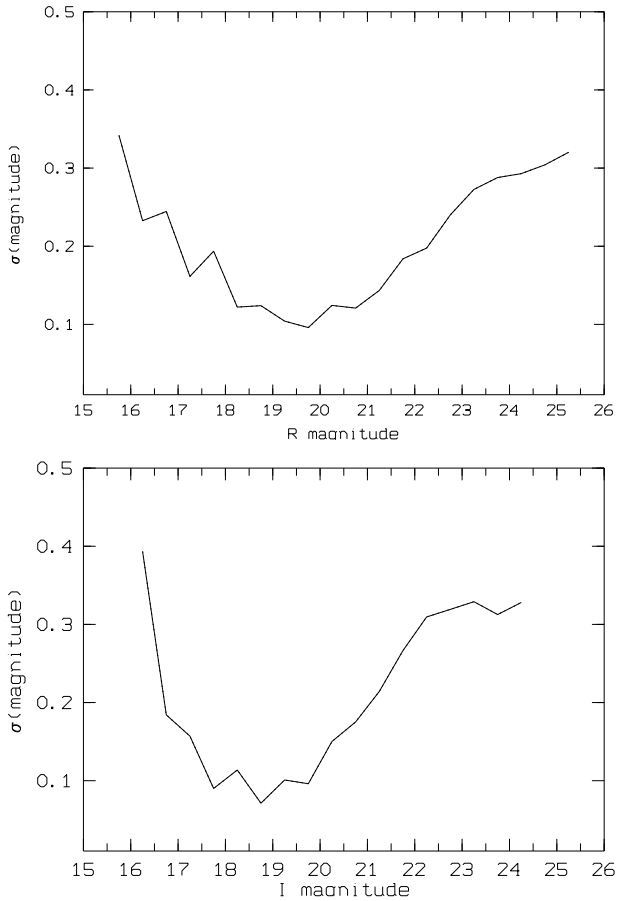


**Fig. 5.** Upper figure: Statistical  $1\sigma$  uncertainty between first epoch and second epoch data on South R field. Lower graph: Statistical  $1\sigma$  uncertainty between I band second epoch data in the common area.

**Table 5.** Fit of the magnitude uncertainty as a function of magnitude deduced from the common areas. This was used to compute uncertainties for individual galaxies: Uncertainty = slope  $\times$  magnitude + constant term.

Magnitude band	validity domain	slope	constant term
B	[20,25.5]	0.0340	-0.5933
V	[20,24.5]	0.0445	-0.8352
R	[20,24]	0.0093	-0.0160
I	[20,23.5]	0.0657	-1.1772

#### 4.6. Magnitude biases

Systematic bias in the magnitudes of catalogued objects could occur as a result of the presence of close neighbors and saturation effects. The effects of each of these is assessed below.

##### 4.6.1. Neighbor contamination

To check this effect on the magnitude determination, we select the objects flagged by SExtractor as having a chance of being biased by at least 0.1 magnitude by a close neighbor. The percentage of such objects, measured in the R

band, is shown in Fig. 6 and appears to be at a relatively constant level close to 15-20%. This tells us that a relatively small fraction of our objects is significantly affected by close neighbors.

##### 4.6.2. Saturation effects

In order to quantify the percentage of objects which could be affected by saturation effects, we select objects flagged by SExtractor as having at least one pixel saturated in their profile. The result is given in Fig. 6 as a function of magnitude and shows that up to  $R=17.5$  objects have a probability to have at least one saturated pixel higher than 50%. The magnitude error is not quantified and depends on the object brightness and morphology and so we chose to check the magnitude of all brighter objects in shallower published data.

We have added published data only if they cover our whole field of view (GP77, Terlevich 2001 and Komiyama 2002) to our catalog of objects brighter than  $R=17.5$  applying the mean magnitude shifts computed in Section 4.7, without color corrections.

In the V band data, objects from the Terlevich et al. (2001) catalog fainter than  $V\sim 14$  should not be saturated and can therefore cover the whole range of our saturated objects.

In the B and R bands, data acquired by Komiyama et al. (2002) are supposed to not be affected by saturation for magnitudes fainter than  $R=14$ . However, we expect that very concentrated objects could still be saturated for magnitudes somewhat fainter than  $R=14$ , and so we chose a conservative approach by using the Komiyama et al. (2002) catalog only between  $R=15.75$  and  $17.5$  and the GP77 catalog for brighter objects.

In summary, all objects in the catalog fainter than  $R=17.5$  come from our CFH12k data. For objects between  $R=15.75$  and  $17.5$ , their R and B magnitudes are taken from Komiyama et al. (2002) or GP77 if the objects are classified as saturated by us. Objects brighter than  $R=15.75$  are taken from GP77 if classified as saturated in our data. Finally, V magnitudes of objects brighter than  $R=17.5$  and classified as saturated are taken from Terlevich et al. (2001).

In total we identified  $\sim 540$  potentially saturated objects in our catalog with  $R<17.5$ , of which 272 are identified as galaxies in the literature. The unidentified objects could be either stars (which are not included in the Komiyama et al. and GP77 catalogs) or galaxies. However, at least half of the  $R<17.5$  objects are stars (see Fig. 15), which are more easily saturated than galaxies, and hence the largest part of the unidentified objects is likely to be stars.

We looked, however, at the 270 unidentified objects in our images and most of them were obviously stars (slightly less than 70%). A smaller subsample was made of compact objects, possibly stars or spheroidal galaxies (slightly less than 30%). Finally, a few galaxies were identified (7

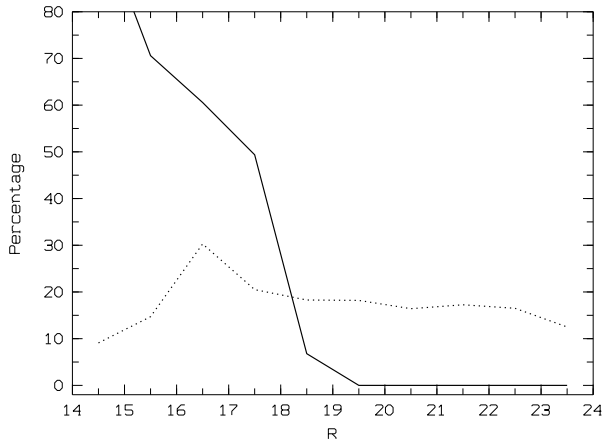


**Fig. 6.** Solid line: percentage of objects with at least one saturated pixel as a function of R magnitude. Dashed line: same for biased magnitudes by 0.1.

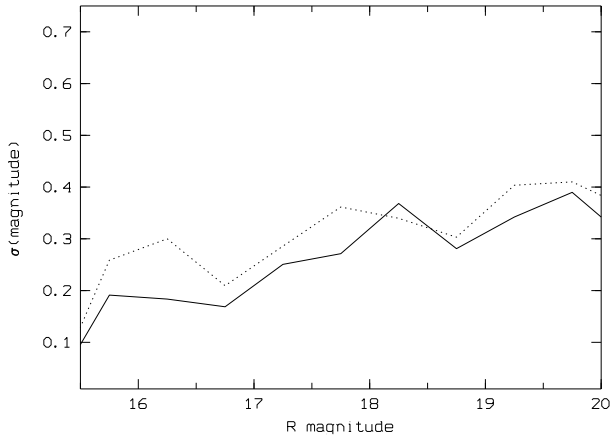


**Fig. 7.** Solid line: statistical  $1\sigma$  error between R GP77 and R CFHT magnitudes, dashed line: B GP77 versus B CFHT magnitudes.

galaxies). We therefore decided to classify as stars all the unidentified objects that were not obviously galaxies. This number of  $\sim 263$  stars is, moreover, in good agreement with the Besançon model star counts (Gazelle et al. 1995).

#### 4.7. Magnitude comparison with other catalogs

We first compared our catalog to the GP77 photographic catalog (up to  $R \sim 19.5$ ) which covers a very large area that encompasses our whole field. The result is given in Fig. 7. The dispersion is lower than 0.4 magnitude at  $R=20$  and close to 0.1 in R and 0.15 magnitude in B at  $R=15.5$ , with the following mean offsets:

$$\begin{aligned} \text{B CFHT} &= \text{B GP77} + 0.20 \\ \text{R CFHT} &= \text{R GP77} + 0.52 \end{aligned}$$

We also compared our results with those of Terlevich et al. (2001) in the V band and Komiyama et al. (2002) in the B and R bands. The results are shown in Figs. 8 and 9. B, V and R data are in good agreement, with a

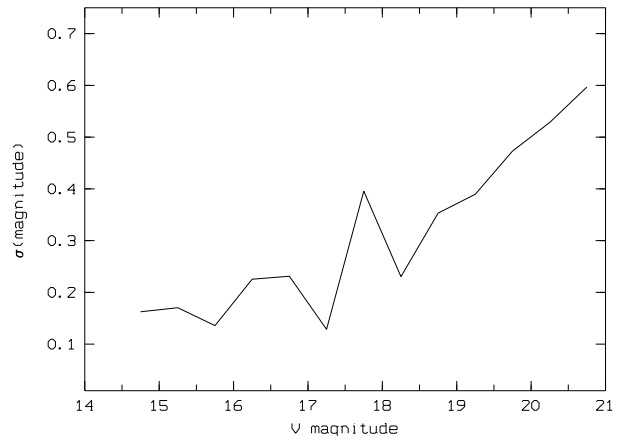


**Fig. 8.** Statistical  $1\sigma$  uncertainties between V magnitudes from Terlevich et al. and from our CFHT observations.

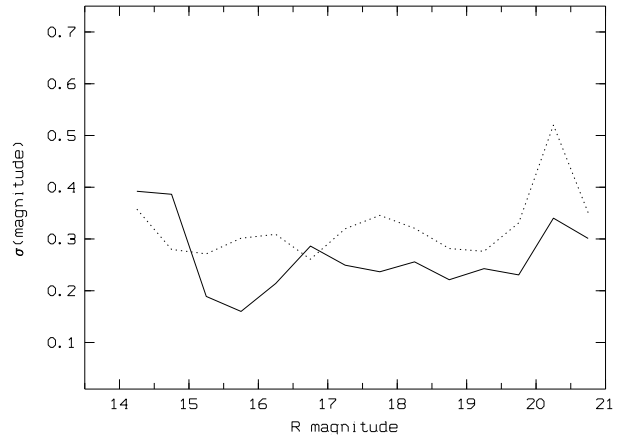


**Fig. 9.** Solid line: statistical  $1\sigma$  uncertainties between R-band magnitudes from Komiyama et al. and our CFHT data, dashed line: statistical  $1\sigma$  uncertainties between Komiyama et al. and CFHT B magnitudes.

dispersion at the bright end close to 0.2 magnitude for V, 0.25 magnitude for R and 0.3 magnitude for B. The mean offsets are:

$$\begin{aligned} \text{B CFHT} &= \text{B Komiyama} - 0.09 \\ \text{V CFHT} &= \text{V Terlevich} + 0.12 \\ \text{R CFHT} &= \text{R Komiyama} + 0.03 \end{aligned}$$

Finally, we compared our results with the CCD observations of Bernstein et al. (1995). The result is shown in Fig. 10. At  $R=20$ , the dispersion is within 0.15 mag for the R band and 0.2 mag for the B band. At the faint end of the catalog ( $R \sim 25$ ) the dispersion is 0.35 in R and 0.45 in B. At our catalog completeness level ( $R \sim 24$ ) the dispersion is 0.25 in R and 0.3 in B. We note that there is a moderate to strong difference in seeing between our data and those of Bernstein et al., since the worst seeing for our data was 1.07 arcsec in B and 0.87 arcsec in R, while that of Bernstein et al. was 1.31 arcsec. This probably explains why we see a rather smooth variation of the dispersion between the Bernstein et al. and our B band

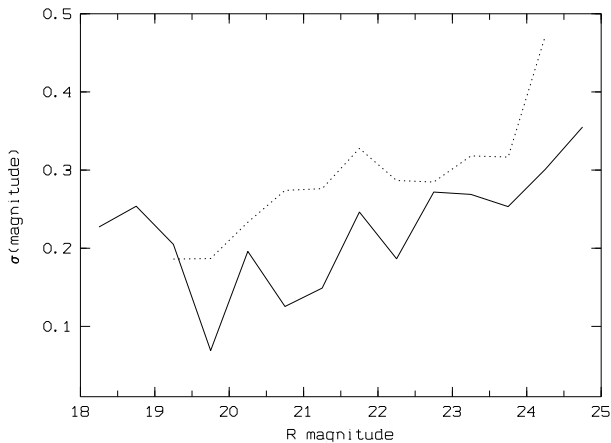


**Fig. 10.** Solid line: statistical  $1\sigma$  uncertainties between R Bernstein et al. and R CFHT magnitudes, dashed line: statistical  $1\sigma$  uncertainties between B Bernstein et al. and B CFHT magnitudes.

magnitudes, while the comparison in the R band shows visible oscillations.

The consistency between our catalog and others allows us to merge some of the data to recover the saturated bright end of our catalog. As we will use external data only for bright galaxies over a rather limited magnitude range, and the mean offsets are small, we do not include color terms from one photometric system to an other.

## 5. Catalog completeness

The catalog completeness has been measured in two ways: by simulations and by comparison with a deeper catalog.

The simulation method adds artificial objects of different shapes and magnitudes to the CCD images and then attempts to recover them by running SExtractor again with the same parameters used for object detection and classification on the original images. In this way, the completeness is measured on the original images and at different locations in the cluster. We investigated the catalog completeness for point-like and faint low surface brightness objects separately. This is because part of the faint galaxy population in clusters consists of faint low surface brightness galaxies (R central surface brightness fainter than 24), which can be nucleated (e.g. Ulmer et al. 1996). These objects are crucial for understanding the cluster physics and, determining how deep we can observe this population by comparison with point like objects, is of major interest.

### 5.1. Simulations for point-like objects

The results at the 90% mean completeness level are summarized in column two of Table 6 for all filters and in the two fields.

An example is given in Fig. 11, which shows how the completeness levels vary from CCD to CCD because of the

QE variations between individual CCDs and because of fluctuations in the diffuse background light due to bright stars and galaxies in the field.

### 5.2. Simulations for low surface brightness objects

We estimated the completeness of our catalog for low surface brightness galaxies using simulated point-like objects with a FWHM of slightly more than 2 arcsec from a Gaussian profile. This is the typical maximal size of a low surface brightness galaxy (e.g. Ulmer et al. 1996) in Coma. This method does not always take into account the true profile of low surface brightness objects in Coma but is a good compromise between simulation simplicity and result accuracy. Results are summarized in column 3 of Table 6 and an example is given in Fig. 12 for the B filter.

### 5.3. Comparison with the Bernstein catalog

Assuming that the Bernstein catalog is 100% complete at our limiting magnitude, we can use it to obtain an independent estimate of the completeness of our catalog. Based on this, we find 90% completeness at R=23.5, which differs from that predicted by our simulations, 90% at 24.5 for point-like objects and 50% at 22.5 for faint low-surface-brightness objects.

There are probably several reasons for the discrepancy. First, faint galaxies are not exactly stellar-like objects and their detection rate is, therefore, lower than for stars. This probably explains part of the difference.

Second, the Bernstein (1995) field is located very close to the two dominant galaxies of the Coma cluster where there is a high level of diffuse light, which can affect the detection of faint objects against this background. The Bernstein image was specifically treated to remove this light and improve the detection rate of the faintest objects. As we do not try to correct our data from diffuse light, this may contribute to the difference in completeness limits.

## 6. Star-galaxy separation

Objects are classified as star-like or galaxies following two criteria both based on the I band data. We used this band because it was reduced in the most homogeneous way on the whole field and was obtained under the best seeing conditions. The price to pay is that not all objects detected in R have an I counterpart (R band data are deeper than I band data). However, as we will limit the star-galaxy separation to I=21, this is not a serious concern as most of the I $\leq$ 21 objects are detected in the 4 bands.

As a first criterion for star-galaxy separation, we use the SExtractor class parameter, which varies from 0 for galaxies to 1 for stars. We classify as stars objects with values greater than 0.98 (e.g. McCracken et al. 2003).

The second criterion comes from the relation between the total magnitude and the central surface brightness for different types of objects. The stellar locus clearly appears up to I $\sim$ 21 on Figs. 13 and 14 showing unambiguously



**Table 6.** 90% and 50% completeness levels for point-like and faint low surface brightness galaxies.

Magnitude	point-like 90%	point-like 50%	low surface brightness 90%	low surface brightness 50%
B North	B=24.75	B=25.5	B=22.0	B=23.25
B South	B=25.	B=26.	B=21.75	B=23.25
V North	V=24.25	V=24.75	V=21.0	V=22.25
V South	V=24.	V=24.5	V=21.25	V=22.25
R North	R=24.	R=24.5	R=20.75	R=21.75
R South	R=24.5	R=25.	R=20.75	R=22.5
I North	R=23.5	R=24.	R=20.5	R=21.5
I South	R=23.25	R=24.	R=20.25	R=21.5

the good quality of the star-galaxy separation up to this magnitude. The lines separation between stars and galaxies were put in by hand in order to optimally separate the stellar and galaxy loci.

For objects between  $I=17$  and  $18.5$ , we did not use the total magnitude / central surface brightness criterion because the separation line starts to classify stars as galaxies around  $I=18.25$  and classify as stars all objects based on the SExtractor class criterion. For objects between  $I=18.5$  and  $21$  we used the second criterion and classified as stars all objects below the heavy solid line in Fig. 13.

Because the North and South data were obtained under different seeing conditions, the criteria were slightly different in the two fields and so we performed the star-galaxy separation individually for each of the fields.

Beyond  $I=21$ , the star-galaxy separation is very unreliable, because of possible confusion of stars with small galaxies (with seeing dominated profiles) and we chose to classify all objects in this range as galaxies.

### 6.1. Star counts: comparison to the Besançon model

Our star counts shown in Fig. 15 agree well with the predictions from the Besançon model for our galaxy (Gazelle et al. 1995 or <http://bison.obs-besancon.fr/modele/>) in the I band and confirm the quality of the star-galaxy separation between  $I=17$  and  $I=21$ . At fainter magnitudes, the predictions show that the contribution of stars is only 10% at  $I=21$  and drops quickly beyond that.

### 6.2. Moving objects and spectroscopically confirmed stars

In order to further check the position of the stellar locus in the surface brightness/total magnitude plots, it is useful to plot known stars in the diagram. One way to do this is to use proper motion to identify stars in the Galactic halo. However, a check of the VizieR database at CDS revealed that there are no published moving stars in the  $I=[19;21]$  range in this field.

We therefore compared our images observed in 2000 to the DSS photographic plate observed in 1955 and to the Bernstein et al. (1995) field observed in 1991, in order to identify moving stars in our fields. Using a simple cross-correlation we select all CFHT objects with a counterpart between 3.4 arcsec (i.e.  $\sim 3$  times the rela-

tive astrometric precision between catalogs) and 15 arcsec in the DSS and between 1.4 arcsec (i.e. 2 times the relative astrometric precision between the catalogs) and 4 arcsec in the Bernstein et al catalog. These upper values limit our search to proper motions smaller than 400 mas/year, a reasonable upper limit (see e.g. the Tycho-2 catalog, Hog et al. 2000). After examining each of these objects and rejecting spurious detections, we were left with two bona fide moving objects in the South field and none in the North field. The first of these is detected from the DSS plate ( $\alpha_{2000}=194.8629^\circ$ ,  $\delta_{2000}=27.6834^\circ$ ,  $I=19.62$ ). The second one is detected from the Bernstein et al. (1995) image ( $\alpha_{2000}=194.8673^\circ$ ,  $\delta_{2000}=27.8909^\circ$ ,  $I=19.67$ ). Additionally, observations reported in Adami et al. (2000) led to the spectroscopic discovery of a third star ( $\alpha_{2000}=194.8149^\circ$ ,  $\delta_{2000}=27.9257^\circ$ ,  $I=19.05$ ) in our fields.

These three objects are well located in the star locus, giving us confidence in the reliability of our star-galaxy separation at least down to  $I\sim 20$ .

## 7. Colors

In order to check the reliability of the photometric spectral energy distributions (SEDs) obtained in our fields, we have compared the observed colors with theoretical expectations derived for two different and well-defined samples of objects: stars and galaxies with known redshifts. Although photometric redshifts and star-galaxy identifications are beyond the scope of the present paper, this section provides a reference on the quality of our SED data from  $\sim 4000 \text{ \AA}$  to  $1 \mu\text{m}$ .

### 7.1. Stars

Synthetic colors for stars have been derived for a variety of spectral types and luminosity classes, using the empirical stellar library of Pickles (1998). We have adopted a detailed modeling for filter transmissions, taking into account the total efficiency of the system as a function of wavelength. Stars have been selected in our catalogs according to the criteria given in Sect. 7 between  $I=17$  and  $21$ . There is a good agreement between synthetic and observed colors of stars, as shown in Fig. 16. On the color-color diagram  $B-V$  vs.  $R-I$ , both the theoretical locus of the observed main sequence and the expected dispersion towards  $B-V \geq 1.2$  are well reproduced by observed stars.

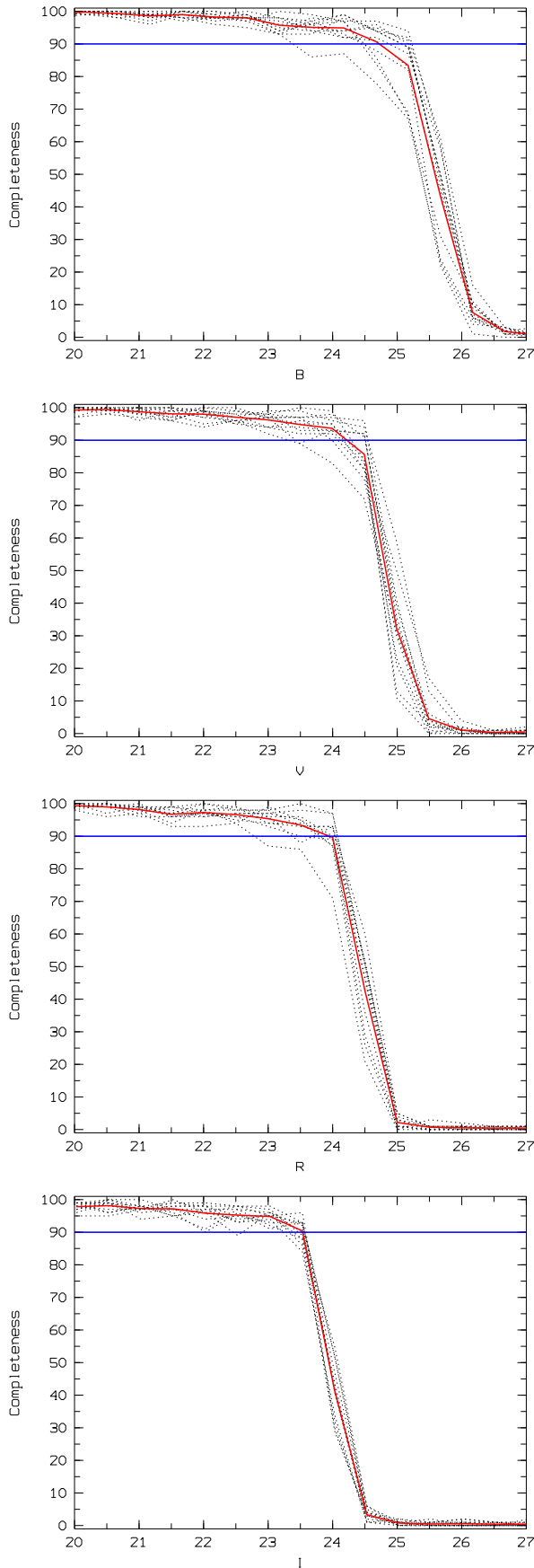


**Fig. 11.** Completeness in percentages in B, V, R and I magnitudes for point-like objects in the North field. The dotted lines show the completeness of individual CCDs, the solid line is the mean completeness for the North field and the solid horizontal line is the 90% completeness level.

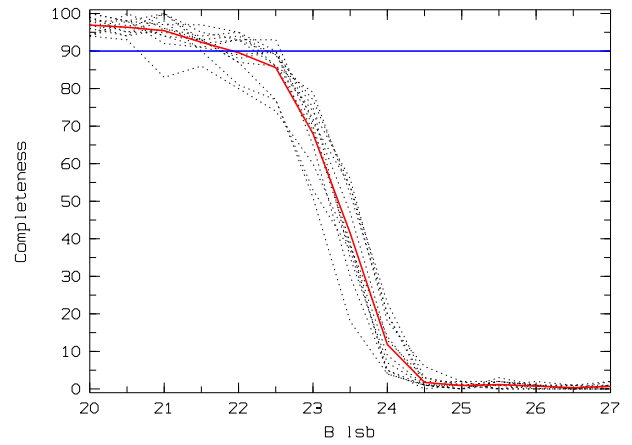


**Fig. 12.** Same as Fig. 11 for the faint low surface brightness galaxies in the North field and in the B band.

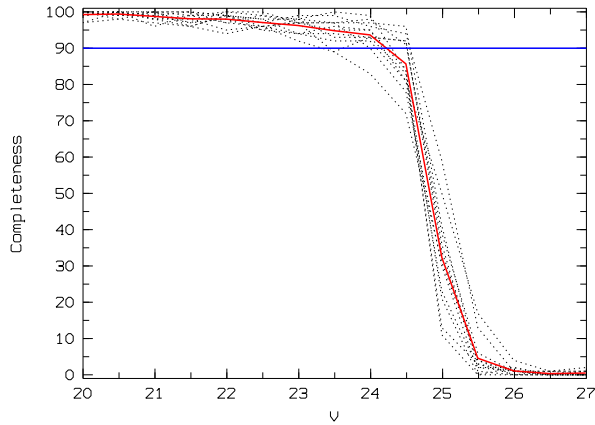


**Fig. 13.** Central I surface brightness versus I total magnitude. Crosses are objects identified as stars by SExtractor with class parameter 0.98 or greater. The heavy solid line shows the star-galaxy separation we chose for the range  $I=[18.5;21]$ . Upper graph: North field. Lower graph: South field.

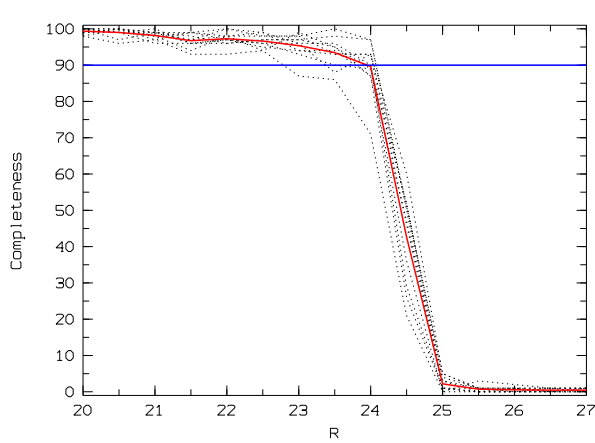


**Fig. 14.** Same as Fig. 13 but in  $I=[18.8;22]$ . The large squares in lower graph are the 3 faintest bona fide stars (determined by external means) in the field.

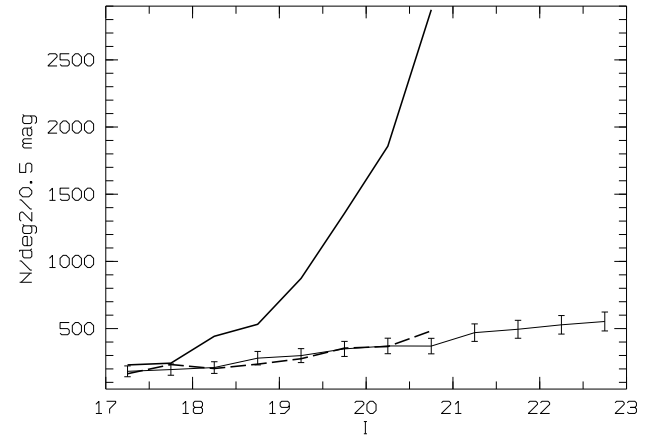
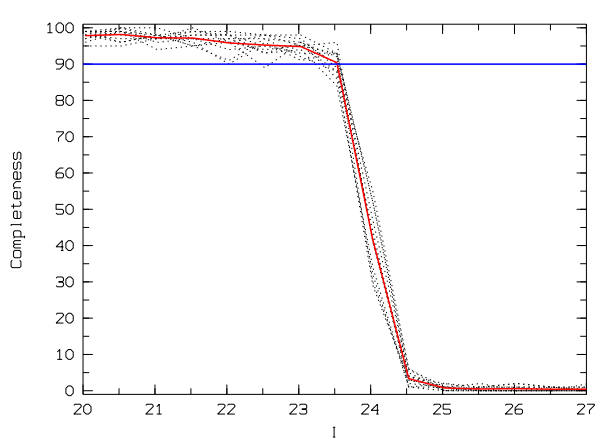


**Fig. 15.** Star counts in our Coma catalog (long-dashed line), star counts from the Besançon model (thin line with error bars) and galaxy counts (solid line). Error bars are at the  $3\sigma$  level.

## 7.2. Galaxies

The set of empirical templates compiled by Coleman, Wu and Weedman (1980) was used to derive representative synthetic colors for galaxies in our photometric system as a function of redshift. The spectro-morphological types considered are the following: E, Sbc, Scd and Im, thus providing a simple representation of the galaxy population in the

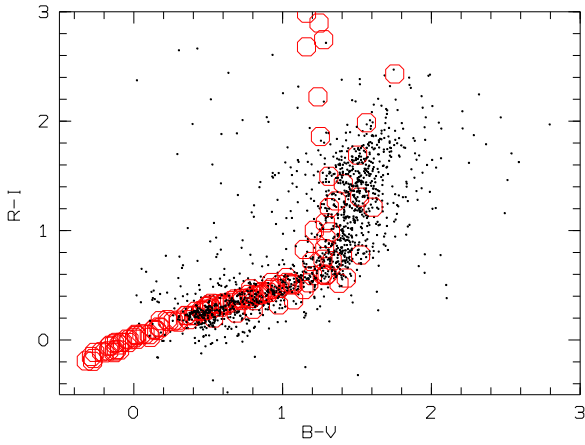


**Fig. 16.** R-I versus B-V for I=[17;21] stars in our catalog (dots), compared to synthetic values derived from the library of Pickles (1998) (large open circles).

local universe. Colors were obtained using the detailed filter transmissions mentioned above for the CFH12K camera, with a simple  $k$ -correction.

A sample of 873 cluster members compiled from the literature (with measured velocities between 4000 and 10000 km/s) is available, as described by Adami et al. (2005b). Although this spectroscopic sample is rather small, observed colors are found to be in good agreement with model predictions. A representative example is given in Fig. 17 for  $B-I$  as a function of redshift. A large majority of cluster galaxies display colors fully compatible with early-type models, and the range of colors spanned by the whole spectroscopic sample is in agreement with simple model expectations. This is particularly true for galaxies morphologically identified as early types from visual inspection (Biviano et al. 1996). It is worth noting that dust reddening has not been considered here, and some objects displaying extremely red colors would need this correction to fit into the scheme. In particular, a moderate intrinsic extinction  $A_V \geq 0.5$  magnitudes ( $E(B-V) \geq 0.12$ , with a Calzetti et al. 2000 reddening law) provides  $B-V \geq 2.5$  when applied to an Sbc template at the Coma redshift, using a simple dust-screen model. Thus, dust extinction could naturally explain the very red colors observed for a few galaxies (less than 10% of the total spectroscopic sample) in Fig. 17 compared to models. Also bright objects with pixels close to the saturation limit could exhibit atypically red colors.

Also bright objects with pixels close to the saturation limit could exhibit atypically red colors.

In summary, the bulk of the spectroscopic sample nicely fits into the expected color-redshift diagrams, and this indicates a good quality of the photometric SEDs for future studies based on SED-fitting techniques.

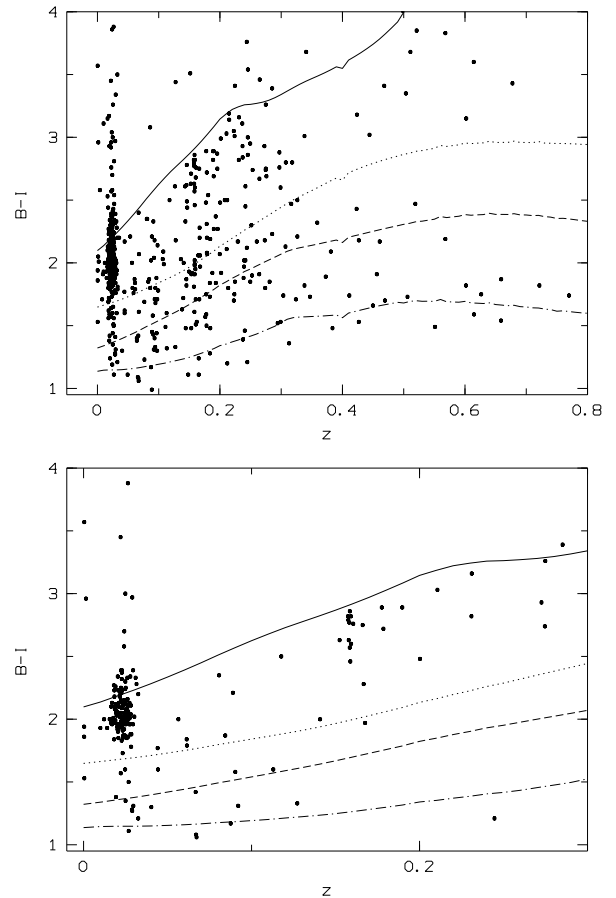


**Fig. 17.** B-I versus redshift for a sample of galaxies with spectroscopic redshifts in this field (from Adami et al. 2005b), compared to simple model expectations derived from Coleman et al. (1980) templates. From top to bottom: elliptical galaxy (solid line), Sbc (dotted line), Scd (long dashed line) and Im (dot-dashed line). Top panel: all galaxies. Bottom panel: galaxies visually classified as early type galaxies according to their morphology.

### 7.3. Red sequence in the Color Magnitude Relation

We also used the spectroscopic sample described in the previous section to investigate the color magnitude re-

**Fig. 18.** Color magnitude relation in the Coma cluster. Small dots: all galaxies on the Coma line of sight. Grey (B&W format) / green (color format) filled circles: Coma members. Black (B&W format) / red (color format) filled circles: early type Coma members. Black (B&W format) / red (color format) solid line: our fitted red sequence. Upper figure: grey (B&W format) / green (color format) solid and dashed lines are the 1 and  $3\sigma$  error envelopes. Lower figure: on an expanded scale, the solid grey (B&W format) / green (color format) line is the  $1\sigma$  error envelope and the two black (B&W format) / red (color format) dashed lines are the red sequences from Secker et al. (1997) and Lopez-Cruz et al. (2004)

lation (B-R versus R, hereafter the CMR) in the Coma cluster and to compare our results with published red sequences in Coma. The Coma cluster is known to exhibit a well defined red sequence (e.g. GP77 or Mazure et al. 1988). The shape of this relation is probably driven by metallicity effects in different mass systems (e.g. Kodama & Arimoto 1997). Massive galaxies can be redder than lower mass systems because they are able to retain more metals and then to form more evolved stars. Early type galaxies in this quite old cluster (e.g. Adami et al. 2005b) therefore form a well defined sequence with a negative slope (faint and low mass early type galaxies retain fewer metals than bright and massive ones and are therefore bluer).

Fig. 18 shows this relation. We fit a red sequence using only galaxies classified as early type galaxies and likely Coma members based on their velocities (between 3500 and 10000 km/s). The relation is:

$$B-R = -(0.045 \pm 0.028) \times R + (2.27 \pm 0.48)$$

The errors are quite large, but this is simply due to the small size of the spectroscopic sample (even if one of the largest available for a cluster of galaxies: Adami et al. 2005b) and to the uncertainties in the visual morphological classification (potentially including late type galaxies in the sample). We also overplot on Fig. 18 the error envelopes at the 1 and  $3\sigma$  levels around this mean relation. Error envelopes were simply computed using the modeled magnitude uncertainties (see Section 4.5) as a function of magnitude.

Several points are noteworthy. First, the red sequence defined in this way is in good agreement with the galaxy distribution in the R/B-R space. The high galaxy density regions in this diagram are well correlated with the red sequence. We also visually inspected the two early type galaxies inside the Coma cluster with extreme B-R values. These two objects (around B-R=2.5, R=16.3 and B-R=0.8, R=18.3) have several velocity measurements in the literature (5 and 4 respectively), all consistent with them being Coma members (7451 km/s and 8043 km/s). These objects must certainly have had peculiar histories that made their B-R colors atypical. They probably experienced dynamical encounters at least for the reddest one which has a peculiar shape in our images. However, discussing the precise evolution of these two objects is beyond the scope of this paper.

Second, the galaxies inside the Coma cluster but without morphological information available in the literature (filled grey circles in Fig. 18) are also very close to this red sequence, defining a relatively narrow relation down to  $R \sim 19$  (consistently with e.g. Adami et al. 2000). What occurs at fainter magnitudes remains uncertain as we do not have deep enough spectroscopy to reach any conclusion (see also Adami et al. 2000).

Finally, our red sequence agrees very well with results published previously in the literature, as shown in Table 7. Some marginal differences exist for the constant terms but are due to slight differences in the B and R filters used by different studies.

**Table 7.** Literature red sequences in the B-R/R sequence.

Authors	Slope	Constant term
present paper	-0.045	2.27
Gladders et al. (1998)	-0.045	-
Lopez-Cruz et al. (2004)	-0.046	2.22
Secker et al. (1997)	-0.056	2.41

Investigations of the faint part of the red sequence are beyond the scope of this paper and will be addressed in a future work.

## 8. Summary and prospects

We have presented and discussed the properties of a catalog of more than 60,000 objects in the Coma cluster based on deep CFHT observations in the B, V, R and I bands and spanning an unprecedented 10 magnitude range in one of the largest  $\sim 0.72 \times \sim 0.82$  deg<sup>2</sup> areas presently available for Coma at this depth. The catalog is complete at the 90% level down to  $R \sim 24$  for stellar-like objects and to  $R \sim 20.75$  for faint low surface brightness (see Sect. 5.2) galaxy-like objects.

Astrometry is accurate to 0.5 arcsec, except for first epoch data on the edges and corners of the CCDs. Magnitude errors are smaller than  $\sim 0.3$  in all bands down to  $R=25$ . Saturation effects on objects brighter than  $I=17.5$  have been removed by using shallower published data. More generally, galaxy magnitudes are in good agreement with published data and the colors of galaxies and stars are in good agreement with synthetic models. The bright part of the CMR agrees well with that derived for galaxies with known redshifts in the Coma cluster, and with previous CMRs published in the literature.

The star-galaxy separation is robust for all objects brighter than  $I=21$ , and the star counts fit the Besançon model very well.

These data have already been used to search for diffuse emission in the Coma cluster (Adami et al. 2005a) and to look for and analyze properties of faint low surface brightness galaxies (Adami et al. 2006). We plan next to use these data to investigate the properties of the different cluster galaxy classes and to derive the luminosity functions of the Coma cluster galaxies in various bands and in various regions of the cluster. This should deepen our knowledge of environmental effects on galaxy luminosity functions, already shown to be strong in Coma (e.g. Lobo et al. 1997).

The catalog described above will be made public by the CENCOS center at <http://cencosw.oamp.fr/>. Individual catalogs for the second epoch R and I band data will also be available upon request.

**Acknowledgements.** The authors thank the referee for useful and constructive comments. We also thank the CFHT and Terapix teams, especially Mireille Dantel-Fort for reducing the second epoch data and the French PNG for financial support. M.J. West acknowledges support from U.S. National Science

Foundation grant AST-0205960.

## References

- Adami C., Ulmer M.P., Durret F. et al. 2000, *A&A* 353, 930
- Adami C., Slezak E., Durret F. et al. 2005a, *A&A* 429, 39
- Adami C., Biviano A., Durret F., Mazure A. 2005b, *A&A* in press, astro-ph/0507542
- Adami C., Scheidegger R., Ulmer M.P., et al. 2006, *A&A* submitted
- Andreon S., Cuillandre J.C., 2002, *ApJ* 569, 144
- Bernstein G.M., Nichol R.C., Tyson J.A., Ulmer M.P., Wittman D. 1995, *AJ* 110, 1507
- Bertin E. & Arnouts S. 1996, *A&AS* 117, 393
- Biviano A., Durret F., Gerbal D. et al. 1996, *A&A* 311, 95
- Biviano A. 1998, Proc. “A new vision of an old cluster: untangling Coma Berenices”, Marseille 17-20 June 1997, Mazure et al. Eds., p. 1, World Scientific, at <http://nedwww.ipac.caltech.edu/level5/Biviano/frames.html>
- Calzetti, D., Armus, L., Bohlin R.C., et al., 2000, *ApJ*, 533, 682
- Castander F.J., Nichol R.C., Merrelli A. et al. 2001 *AJ*, 121, 2331
- bibitem[1980]CWW Coleman, D.G., Wu, C.C., Weedman, D.W. 1980, *ApJS* 43, 393
- Cuillandre J.C., Mellier Y., Dupin, J.P. et al. 1996 *PASP*, 108, 1120
- Cuillandre J.C., Luppino G.A., Starr B.M., Isani S. 2000, in Proc. SPIE “Optical and IR telescope instrumentation and detectors”, Vol. 4008, 1010
- Durret F., Adami C. & Lobo C. 2002, *A&A* 393, 439
- Gazelle F., Robin A. & Goidet-Devel B. 1995, *Vistas in Astronomy* 39, 105
- Gladders M.D., Lopez-Cruz O., Yee H.K.C., Kodama T. 1998, *ApJ* 501, 571
- Godwin J.G. & Peach J.V. 1977, *MNRAS* 181, 323 (GP77)
- Hog E., Fabricius C., Makarov V.V. et al. 2000, *A&A* 355, L27
- Kalirai J.S., Richer H.B., Fahlman G.G. et al. 2001, *ApJ* 122, 257
- Kodama T., Arimoto N., 1997, *A&A* 320, 41
- Komiyama Y., Sekiguchi M., Kashikawa N. et al. 2002, *ApJS* 138, 265
- Landolt A.U. 1992, *AJ* 104, 340
- Lobo C., Biviano A., Durret F. et al. 1997, *A&A* 317, 385
- Lopez-Cruz O., Barkhouse W.A., Yee H.K.C. 2004, *ApJ* 614, 679
- Luppino, Gerard A., Bredthauer R.A., Geary J.C. 1994, Proc. SPIE Vol. 2198, p. 810
- Mazure A., Proust D., Mathez G., Mellier Y., 1988, *A&AS* 76, 339
- McCracken H.J., Radovich M., Bertin E. et al. 2003, *A&A* 410, 17
- Mellier, Y., Mathez G., Mazure A., Chauvineau B., Proust D. 1988, *A&A* 199, 67
- Pickles, A. J. 1998, *PASP* 110, 863
- Saglia R.P., Bertschinger E., Baggley G. et al. 1993, *MNRAS* 264, 961
- Savine C. 2002, PhD, Université de Provence
- Schlegel D.J., Finkbeiner D.P., Davis M. 1998, *ApJ* 500, 525
- Secker J., Harris W.E., Plummer J.D., 1997, *PASP* 109, 1377
- Terlevich A.I., Caldwell N., Bower R.G. 2001, *MNRAS* 326, 1547
- Ulmer M.P., Bernstein G.M., Martin D.R. et al. 1996, *AJ* 112, 2517

This figure "3810f1.jpg" is available in "jpg" format from:

<http://arxiv.org/ps/astro-ph/0606439v1>

This figure "3810f131.jpg" is available in "jpg" format from:

<http://arxiv.org/ps/astro-ph/0606439v1>

This figure "3810f132.jpg" is available in "jpg" format from:

<http://arxiv.org/ps/astro-ph/0606439v1>



This figure "3810f141.jpg" is available in "jpg" format from:

<http://arxiv.org/ps/astro-ph/0606439v1>

This figure "3810f142.jpg" is available in "jpg" format from:

<http://arxiv.org/ps/astro-ph/0606439v1>

This figure "3810f181.jpg" is available in "jpg" format from:

<http://arxiv.org/ps/astro-ph/0606439v1>

This figure "3810f182.jpg" is available in "jpg" format from:

<http://arxiv.org/ps/astro-ph/0606439v1>